Structural study of bismuth ferrite $BiFeO_3$ by neutron total scattering and the reverse Monte Carlo method

Juan Du, Anthony E. Phillips, Donna C. Arnold, David A. Keen, Matthew G. Tucker and Martin T. Dove

Published version information

Citation: J Du et al. "Structural study of bismuth ferrite $BiFeO_3$ by neutron total scattering and the reverse Monte Carlo method." Physical Review B, vol. 100, no. 10 (2019): 104111.

DOI: 10.1103/PhysRevB.100.104111

Structural study of bismuth ferrite $BiFeO_3$ by neutron total scattering and the reverse Monte Carlo method

Juan Du and Anthony E. Phillips
School of Physics and Astronomy, Queen Mary University of London, Mile End Road, London E1 4NS, United Kingdom

Donna C. Arnold
School of Physical Sciences, University of Kent, Canterbury, Kent CT2 7NH, United Kingdom

David A. Keen
ISIS Facility, Rutherford Appleton Laboratory, Harwell Campus, Didcot, Oxfordshire OX11 0QX, United Kingdom

Matthew G. Tucker
Oak Ridge National Laboratory, Neutron Scattering Division, 1 Bethel Valley Road, Oak Ridge, Tennessee 37831, USA

Martin T. Dove*
Department of Physics, School of Sciences, Wuhan University of Technology, 205 Luoshi Road, Hongshan district, Wuhan, Hubei 430070, People's Republic of China; College of Computer Science and College of Physical Science & Technology, Sichuan University, Chengdu 610065, People's Republic of China; and School of Physics and Astronomy, Queen Mary University of London, Mile End Road, London E1 4NS, United Kingdom

(Received 23 May 2019; revised manuscript received 21 August 2019; published 16 September 2019)

We report a study of the atomic structure of the multiferroic material bismuth ferrite $BiFeO_3$ using neutron total scattering measurements coupled with analysis using the Reverse Monte Carlo method. We have examined average neighboring interatomic distances and local coordination environments, together with their fluctuations, for temperatures between 16 and 800 K (the sample decomposed at higher temperatures). There is little change in the average structure as a function of temperature, but the results show unusually large thermal motion at higher temperatures. No anomalous behavior is seen within this range, suggesting that the anomalies reported to occur below room temperature most likely arise due to effects associated with surfaces and interfaces.

DOI: 10.1103/PhysRevB.100.104111

I. INTRODUCTION

Bismuth ferrite, $BiFeO_3$, is the most widely studied multiferroic ceramic, primarily because it exhibits both magnetic ($T_N \sim 630$ K) and ferroelectric ($T_C \sim 1100$ K) ordering at room temperature [1]. $BiFeO_3$ has the perovskite structure, with the Fe^{3+} cation occupying the octahedral site and the Bi^{3+} cation on the cuboctahedral sites coordinated to 12 oxygen anions, as shown in Fig. 1.

At room temperature bismuth ferrite crystallizes in the α phase with rhombohedral symmetry, polar space group $R3c$, with the FeO_6 octahedra rotated in an antiphase arrangement about the rhombohedral threefold axis (Glazer notation $a^-a^-a^-$). Both cations are displaced from the center of symmetry along the $[001]_h$ axis of the hexagonal unit cell (corresponding to the $[111]_c$ axis of the parent cubic phase) [1,2], with the Bi^{3+} displacement being largest due to the stereoactive lone pair. Below T_N the magnetic moments of Fe^{3+} order into a complex long-range incommensurate spin cycloid propagating in the $[110]_h$ direction with a periodicity of approximately 620 Å [3]. It is now generally accepted that at T_C $BiFeO_3$ undergoes a first-order phase transition to an orthorhombic β phase with nonpolar $Pbnm$ symmetry [4].

Above 1198 K $BiFeO_3$ adopts the γ phase, the symmetry of which continues to be debated. Initially it was suggested that γ-$BiFeO_3$ adopts the aristotype cubic perovskite $Pm\bar{3}m$ symmetry [5]. However, neutron-diffraction experiments suggest that the γ phase may retain orthorhombic symmetry [6]. High-temperature studies are usually compromised as a result of the thermal instability of $BiFeO_3$. It has been demonstrated that the expected decomposition products are marginally more thermal dynamically stable in the temperature range 720–1040 K [7,8]. More recently differential scanning calorimetry measurements have suggested that $BiFeO_3$ is kinetically unstable above T_C with the β-γ phase transition overlapping the peritectic decomposition [9]. It was also suggested that the structural phase transitions are interlinked and kinetically controlled, and thus dependent on the heating rate. As a result the onset of decomposition of $BiFeO_3$ can occur significantly below the peritectic decomposition temperature, and is somewhat dependent on experimental conditions. This is consistent

*Corresponding author: martin.dove@qmul.ac.uk

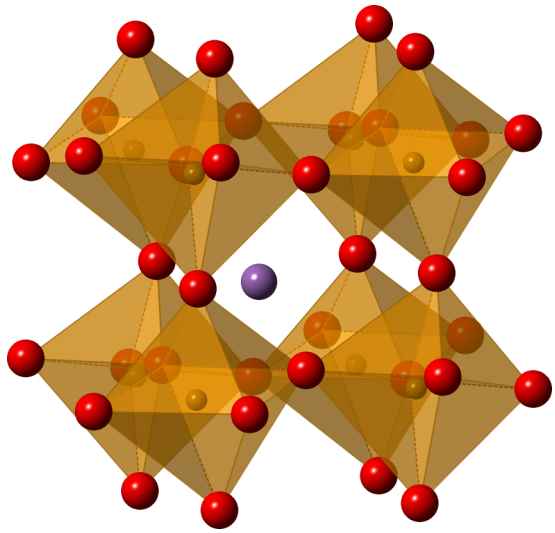

FIG. 1. Structural representation of $BiFeO_3$ in the polar α phase with space group $R3c$. The Fe ions and FeO_6 octahedra are represented by the brown spheres and polyhedra respectively, and the oxygen and bismuth ions are shown as red and purple spheres respectively. Structure diagrams in this paper were generated with the CRYSTALMAKER software [10].

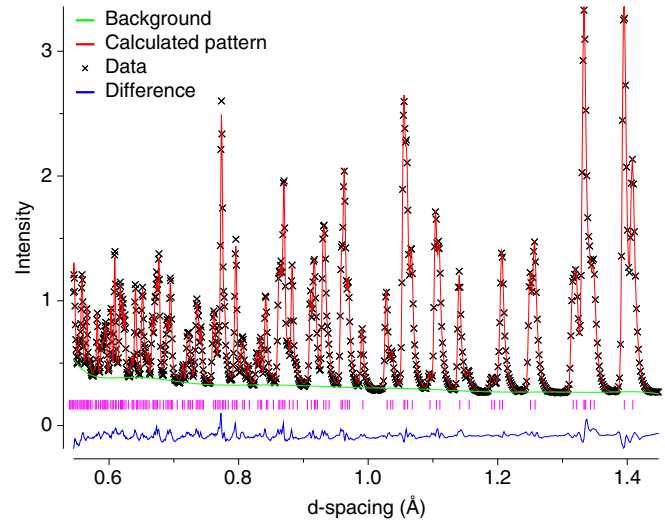

FIG. 2. Example of the quality of the Rietveld refinement of the crystal structure of $BeFeO_3$ from data collected in this study. Here we show a portion of the data from the 90° bank at a temperature of 161 K. Positions of Bragg reflections are shown as the short vertical magenta lines.

with the difficulty to obtain a pure γ phase in diffraction experiments [4–6].

Inelastic neutron spectroscopy experiments conducted between 200 and 750 K exhibited a broadening of the whole excitation spectrum with increasing temperature, which was interpreted in terms of large-amplitude anharmonic motions of Bi and O ions [11]. An anomaly in the Bi-dominated modes around T_N was interpreted as strong evidence for spin-phonon coupling. A more recent inelastic study performed between 300 and 700 K revealed no significant changes in the dynamic response with temperature [12], although broadening of the energy linewidths on heating towards T_N was observed as in Ref. [11], leading to the suggestion that the low-energy lattice dynamics and magnetic order are coupled [11,12].

The low-temperature behavior of $BiFeO_3$ remains the subject of much debate within the literature. No significant changes in the long-range nuclear (atomic) or magnetic structures with varying temperature have been reported in crystallographic studies of single crystal and powder samples of the bulk phases [4,13,14]. On the other hand, anomalous features have been reported in the Raman spectra at multiple temperatures between 140 and 250 K [1,15–17]. Since crystallographic measurements are sensitive to the average structure of the bulk material, there are broadly two possible explanations for this discrepancy. First, many of these studies rely on point analysis of Raman spectra. The position and intensity of a particular mode can be critically dependent on the domain orientation such that features may not necessarily arise as a result of temperature dependence but rather experimental control [2,18]. Alternatively these anomalies may not be due to the bulk structure at all, and instead may arise from grain boundaries with polar character or from the existence of surface phase transitions [19]. Indeed, Domingo *et al.* have suggested the presence of a 5-nm surface and a subsurface layer with a thickness of around 320 nm, both of which behave differently, electrically and structurally, to the bulk [20,21]. Second, the *local* structure may be more complex than the crystallographic average structure suggests. A recent neutron-diffraction and inelastic-scattering study on $BiFeO_3$ nanomaterials [22] suggests that the FeO_6 octahedra become more anisotropic over a narrow range of temperatures around 205 K. Small concomitant changes in the magnetic sublattice were attributed to a spin rearrangement; the inelastic-scattering data show anomalies in the widths of the magnetic features, indicative of slow spin dynamics below 205 K.

One way to approach this puzzle is to investigate the local structure of $BiFeO_3$ directly. To date local structure studies have primarily been limited to room temperature x-ray-absorption spectroscopy and x-ray pair distribution function (PDF) performed as part of comparative doping studies [23–29]. PDF studies at room temperature have been performed on $BiFeO_3$-$PbTiO_3$ solid solutions [30] and La/Tb-doped $BiFeO_3$ [25]. However, up to now no variable temperature PDF studies have been performed on undoped $BiFeO_3$.

In this paper we describe a variable-temperature neutron PDF study of undoped $BiFeO_3$ with analysis using the Reverse Monte Carlo (RMC) method. This approach, uniquely, is able to give simultaneous information about average crystal structure and local fluctuations in the atomic arrangement. The key objective of this work is to examine fluctuations in the structure across the temperature range from 16 to 800 K, particularly to see if these show any signs of the various anomalies previously reported, and to explore any possible link between magnetism and ferroelectricity. Unfortunately, while this temperature range encompasses T_N, it falls short of T_C due to problems of sample stability. Nevertheless, the results here show robustly the growth of large structural fluctuations while the average structure remains surprisingly constant and consistent across the whole temperature range.

TABLE I. Cell parameters and atomic fractional coordinates of $BiFeO_3$ refined from Rietveld refinement in this study; Bi has fractional coordinates 0,0,0 (the value $z = 0$ was not set by symmetry, since the space group $R3c$ has no natural origin, but was chosen to place the Bi atom at the origin of the unit cell), and Fe has fractional coordinates 0, 0, z. Standard deviations are given for the last significant figures in brackets. The roman numerals beside the temperature values differentiate separate sequences on data, with two separate runs in the furnace (II and III) and one in the close-cycle refrigerator (I).

T (K)	a (Å)	c (Å)	Fe z	O x	O y	O z
16 (I)	5.57227(7)	13.8354(3)	0.22031(10)	0.44110(27)	0.01806(30)	0.95165(14)
96 (I)	5.57338(6)	13.8414(3)	0.22029(10)	0.44113(27)	0.01794(30)	0.95166(15)
161 (I)	5.57505(7)	13.8498(3)	0.22034(10)	0.44109(27)	0.01776(31)	0.95174(15)
236 (I)	5.57736(7)	13.8601(3)	0.22041(10)	0.44094(27)	0.01752(31)	0.95186(15)
283 (I)	5.57884(6)	13.8661(3)	0.22051(10)	0.44100(26)	0.01742(30)	0.95197(15)
291 (III)	5.57911(7)	13.8684(3)	0.22073(10)	0.44000(27)	0.01720(31)	0.95243(16)
294 (II)	5.57925(6)	13.8689(3)	0.22056(10)	0.44050(27)	0.01711(31)	0.95214(15)
373 (III)	5.58292(6)	13.8832(3)	0.22099(10)	0.44044(25)	0.01719(29)	0.95276(15)
473 (III)	5.58832(5)	13.9028(2)	0.22131(8)	0.44160(21)	0.01732(25)	0.95305(13)
572 (III)	5.59438(4)	13.9239(2)	0.22162(6)	0.44407(16)	0.01793(19)	0.95323(10)
600 (II)	5.59627(4)	13.9301(2)	0.22155(6)	0.44449(16)	0.01760(18)	0.95301(9)
627 (III)	5.59805(3)	13.9366(1)	0.22170(5)	0.44671(13)	0.01863(15)	0.95307(8)
662 (III)	5.60045(3)	13.9446(1)	0.22179(5)	0.44838(13)	0.01906(15)	0.95302(7)
700 (II)	5.60339(3)	13.9528(1)	0.22189(5)	0.44789(14)	0.01851(16)	0.95314(8)
798 (III)	5.60996(3)	13.9688(1)	0.22241(5)	0.44949(14)	0.01934(16)	0.95388(9)

We will show that neither the average structure nor the local fluctuations show features that reflect the previously reported anomalies or changes in the magnetic order.

II. EXPERIMENTAL METHODS AND DATA ANALYSIS

A. Experimental procedures: Sample and neutron-scattering measurements

$BiFeO_3$ was synthesized using the same methods we have previously reported [4,6]. Briefly, stoichiometric ratios of Bi_2O_3 (Sigma Aldrich, 99.9% purity) and Fe_2O_3 (Sigma Aldrich, purity above 99%) were ground together thoroughly. A 6-mol % excess of Bi_2O_3 was added in order to mitigate against the loss of bismuth during the reaction. The material was heated to 800 °C with a heating rate 10 °C/min, and held at this temperature for 5 h. The resulting powder was leached in 2.5-M HNO_3 with continuous stirring before being washed with double-distilled H_2O and dried at 400 °C (1 h). Phase purity was confirmed by powder diffraction using a Bruker D8 Advance diffractometer using Cu $K\alpha_1$ radiation (40 kV and 40 mA, $\lambda = 1.5406$ Å, 2θ range 10–70°).

Neutron total scattering measurements were performed using the GEM instrument at the ISIS spallation neutron scattering facility [31]. This provides high-quality data to high values of Q, up to 50 $Å^{-1}$, although oscillations in $i(Q)$ had already decayed by smaller values of Q as seen in data shown later in this paper. High values of Q permit better resolution for the structural models in real space, with resolution given

TABLE II. Atomic displacement parameters $100 \times U_{ij}$ ($Å^2$) refined from Rietveld refinement. For Bi $U_{11} = U_{22}$ and $U_{13} = U_{23} = 0$. U_{ij} units are in $Å^2$. Standard deviations are given for the last significant figures in brackets. As in Table I the roman numerals indicate the sets of data in different experimental runs.

T (K)	Bi U_{11}	Bi U_{12}	Bi U_{33}	Fe U_{iso}	O U_{11}	O U_{12}	O U_{13}	O U_{22}	O U_{23}	O U_{33}
16 (I)	0.19(3)	0.092(1)	0.05(5)	0.13(2)	−0.03(4)	0.06(4)	0.06(4)	0.30(5)	0.01(4)	0.34(4)
96 (I)	0.37(4)	0.184(1)	0.14(5)	0.21(3)	0.01(4)	0.07(4)	0.09(4)	0.34(5)	0.01(4)	0.42(4)
161 (I)	0.53(4)	0.267(2)	0.23(5)	0.29(3)	0.06(5)	0.08(5)	0.11(4)	0.37(5)	0.01(5)	0.52(5)
236 (I)	0.72(4)	0.361(2)	0.32(6)	0.38(3)	0.15(5)	0.09(5)	0.14(5)	0.41(5)	0.01(5)	0.68(5)
283 (I)	0.83(4)	0.416(2)	0.38(6)	0.43(3)	0.21(5)	0.10(5)	0.15(5)	0.44(5)	0.00(5)	0.76(5)
291 (III)	0.86(5)	0.431(2)	0.38(7)	0.41(3)	0.07(5)	0.00(5)	0.16(5)	0.29(6)	−0.01(5)	0.81(6)
294 (II)	0.90(4)	0.449(2)	0.41(6)	0.46(3)	0.20(5)	0.08(5)	0.16(5)	0.42(6)	0.00(5)	0.83(5)
373 (III)	1.11(5)	0.555(2)	0.56(7)	0.52(3)	0.27(5)	0.02(5)	0.17(5)	0.34(6)	−0.03(5)	1.02(6)
473 (III)	1.40(4)	0.700(2)	0.75(6)	0.62(3)	0.60(5)	0.06(5)	0.16(5)	0.43(5)	−0.09(5)	1.26(5)
572 (III)	1.68(3)	0.842(1)	0.96(5)	0.71(2)	1.10(4)	0.15(4)	0.08(4)	0.55(4)	−0.20(4)	1.45(4)
600 (II)	1.82(3)	0.912(1)	0.99(4)	0.77(2)	1.35(4)	0.29(4)	0.09(4)	0.73(4)	−0.20(3)	1.51(4)
627 (III)	1.81(3)	0.898(1)	1.04(4)	0.73(2)	1.53(4)	0.26(4)	0.00(4)	0.67(3)	−0.28(3)	1.44(4)
662 (III)	1.88(3)	0.939(1)	1.08(4)	0.75(2)	1.81(4)	0.32(4)	−0.06(4)	0.75(3)	−0.34(3)	1.41(4)
700 (II)	2.14(3)	1.070(1)	1.18(4)	0.86(2)	2.02(4)	0.44(4)	−0.02(4)	0.94(4)	−0.33(3)	1.60(4)
798 (III)	2.46(3)	1.228(1)	1.41(5)	0.93(2)	2.32(4)	0.38(4)	−0.12(5)	0.96(4)	−0.48(3)	1.81(4)

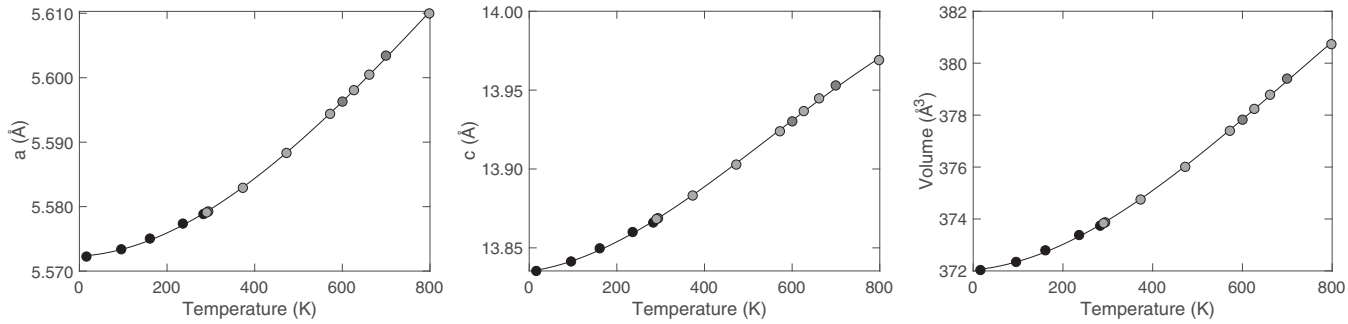

FIG. 3. The refined lattice parameters of $BiFeO_3$ as functions of temperature from Rietveld refinement of the data obtained in this study. Different fill colors for the data points reflect the different data runs. The curves are guides to the eye obtained by fitting third-order polynomials; the sigmoidal shape for c is consistent with more extensive data reported previously [14]. In each graph the error bars are smaller than the size of the data symbols.

as $\Delta r = 2\pi/Q_{\max}$. The range of Q available to the experiment corresponds to a practical range of neutron wavelengths of 0.15–2 Å, which enables energy transfers that correspond to a full integration over all energy transfers implicit in the formulation of the scattering function $i(Q)$ from the full dynamical scattering factor. Thus the configurations in the RMC analysis will be sensitive to the full range of phonon excitations in $BiFeO_3$.

The powder sample was loaded into a cylindrical vanadium can of 8 mm diameter. Total scattering data were obtained in two rounds of experiments performed at different times. The first round enabled data collection at temperatures of 16, 96, 161, 236, and 283 K with the sample in a closed-cycle refrigerator (CCR) and 294, 600, and 700 K with the sample in a furnace [32]. The second round enabled data collection at temperatures of 291, 373, 473, 572, 627, 662, and 798 K in a furnace [33]. Measurement times at each temperature were around 6 h, corresponding to a total proton flux of around 900 μA h.

We found that the nominal temperature of 800 K was the highest temperature we could achieve in these experiments. With the long run times required for these measurements, together with holding the sample in a vacuum rather than air, heating above 800 K led to the formation of decomposition products (such as $Bi_2Fe_4O_9$), as seen in the diffraction data. This is not unusual in $BiFeO_3$ as has been discussed elsewhere [7,8]. The sample was replaced by a fresh sample taken from the same synthesis batch for subsequent measurements after the first signs of decomposition; diffraction data showed no decontamination products in any of the data sets analyzed and presented here.

Data were also collected in each round on an empty instrument, then with the sample environment equipment without sample can, and finally with the sample environmental equipment with an empty sample can, in order to account for additional scattering processes and beam attenuation. A long measurement of the scattering from a vanadium rod was performed for data normalization and calibration of the instrument detectors.

B. Rietveld refinement

The raw diffraction data were processed to form a set of data for Rietveld refinement using the MANTID software [34]. Rietveld refinement on the data was performed using the GSAS software [35] with the EXPGUI interface [36].

The refinements were performed using GSAS lineshape 2 (see the manual [35] for explanation). Instrumental parameters used in the refinement were taken from in-house calibration runs. There is, however, a problem with using three different data sets (one with the CCR, two with furnaces) in that in each case the sample position is slightly displaced from the center in a different way. This has a small but noticeable effect on the refined lattice parameters. In fact GSAS has a parameter to account for this (called "DIFC"). To bring the three data sets into consistency we followed the strategy of refining profile parameters associated with the sample at the lowest-temperature data and then holding these fixed in the refinements of all other data. We then compared the three data sets around room temperature. The lattice parameters for the two room-temperature measurements in the furnace were taken from the refinements of the CCR data (using a simple polynomial fit to the data to enable extrapolation to the actual temperatures to account for the small differences in temperature between three data sets at nominally room temperature). Keeping the lattice parameter fixed, the sample displacement parameter was refined, and this was then held fixed in the refinements of higher-temperature data.

C. Total scattering and the Reverse Monte Carlo method

The total scattering structure factor $i(Q)$ was obtained from the total scattering data after correcting for scattering and attenuation by the sample can and sample environment, and the the detectors normalized by the measurement of incoherent scattering from the vanadium rod. We used the GUDRUN code [37] for this task. The maximum value of Q in the data processing was set to be 40 Å^{-1} for all the temperatures.

The structure factor is related to the partial atomic pair distribution functions $g_{mn}(r)$ through the standard relation:

$$i(Q) = 4\pi\rho \int_0^\infty \sum_{m,n} c_m c_n b_m b_n r^2 [g_{mn}(r) - 1] \frac{\sin(Qr)}{Qr}\, dr, \tag{1}$$

where $g_{mn}(r)$ is defined such that the number of atoms of type n lying within a spherical shell of radius r and thickness dr centered on an atom of type m is equal to $4\pi c_n \rho r^2 g_{mn}(r)$, with ρ denoting the total number of atoms per unit volume, and c_n

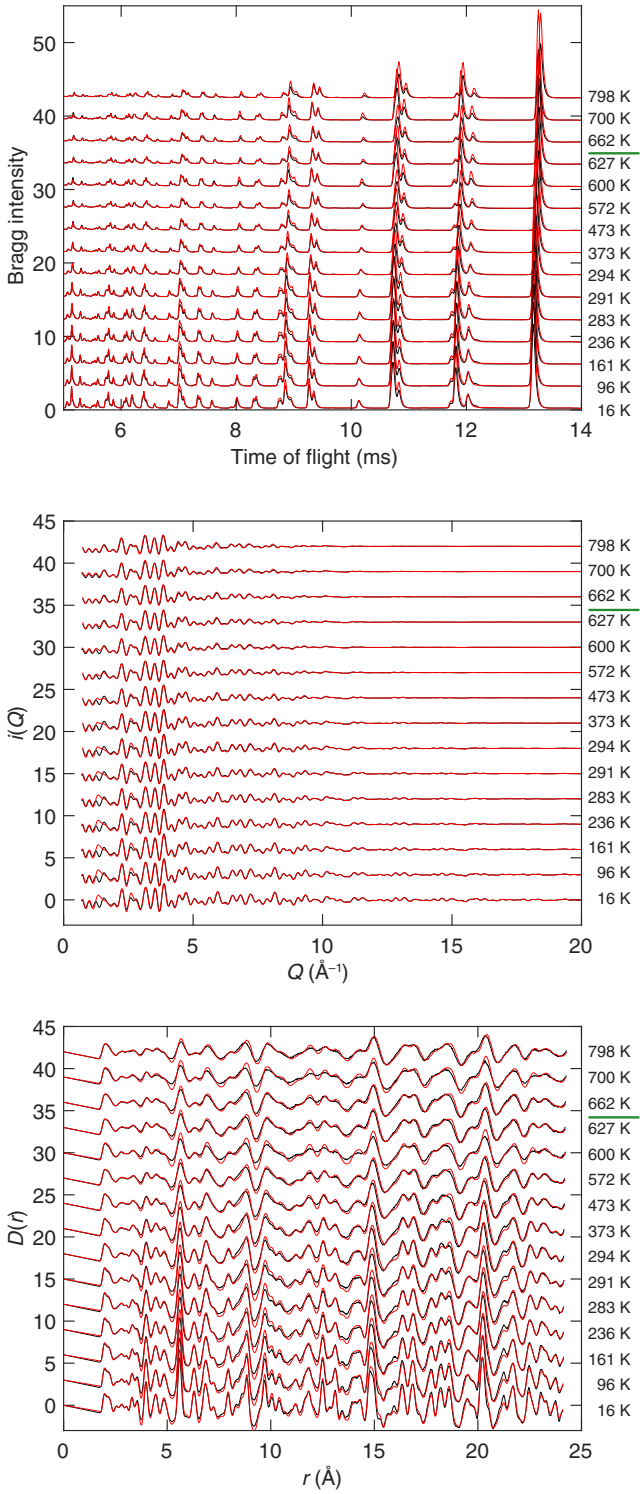

FIG. 4. Suite of data used in the Reverse Monte Carlo modeling, showing the Bragg diffraction data (top), total scattering data (middle), and pair distribution function (bottom). In each case the data are shown as black and the RMC calculation as red. Temperatures of the data are indicated on the right. In each graph data for different temperatures are vertically displaced sequentially by an equal amount. The horizontal lines in the temperature labels separate the temperatures in the magnetically ordered ($T > 630$ K) and disordered ($T < 630$ K) phases.

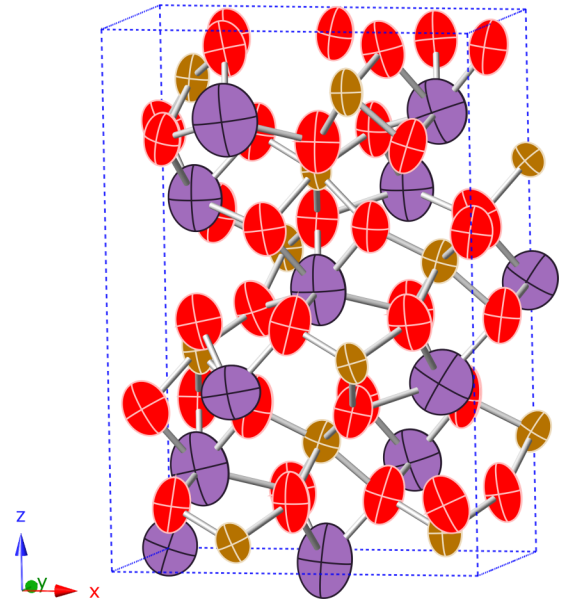

FIG. 5. Average structure with ellipsoid-shape atoms reflecting the amplitudes of anisotropic atomic vibrations at 473 K (Fe in orange, O in red, and Bi in purple).

denoting the fraction of all atoms of type n. We define the overall pair distribution function as

$$D(r) = 4\pi\rho r \sum_{m,n} c_m c_n b_m b_n [g_{mn}(r) - 1]. \tag{2}$$

The functions $i(Q)$ and $D(r)$ are linked through a pair of Fourier sine transforms, which follow from the above definitions:

$$Qi(Q) = \int_0^\infty D(r)\sin(Qr)\,dr \tag{3}$$

and

$$D(r) = \frac{2}{\pi}\int_0^\infty Qi(Q)\sin(Qr)\,dr. \tag{4}$$

$D(r)$ is our function of choice to represent the pair distribution function, in part because as the direct Fourier transform from the analysis presented in the above equations the errors will propagate more or less uniformly across the transform, and in part because $D(r)$ emphasizes the higher-r data more than the functions $g_{mn}(r)$ as a result of the multiplicative factor of r. Although GUDRUN can generate the $D(r)$ function, in this work we performed the Fourier transforms using the STOG program from the ATLAS data analysis suite [38], in part because we chose to use a modification function in the Fourier transform to reduce the effect of termination ripples associated with a finite maximum value of Q, $Q_{\max}$, and to reduce the effects of noise in $Qi(Q)$ at high Q. Thus our transform is

$$D(r) = \frac{2}{\pi}\int_0^{Q_{\max}} M(Q)Qi(Q)\sin(Qr)\,dr \tag{5}$$

where, following the procedure proposed by Lorch [39,40], $M(Q) = \sin(\pi Q/Q_{\max})/(\pi Q/Q_{\max})$.

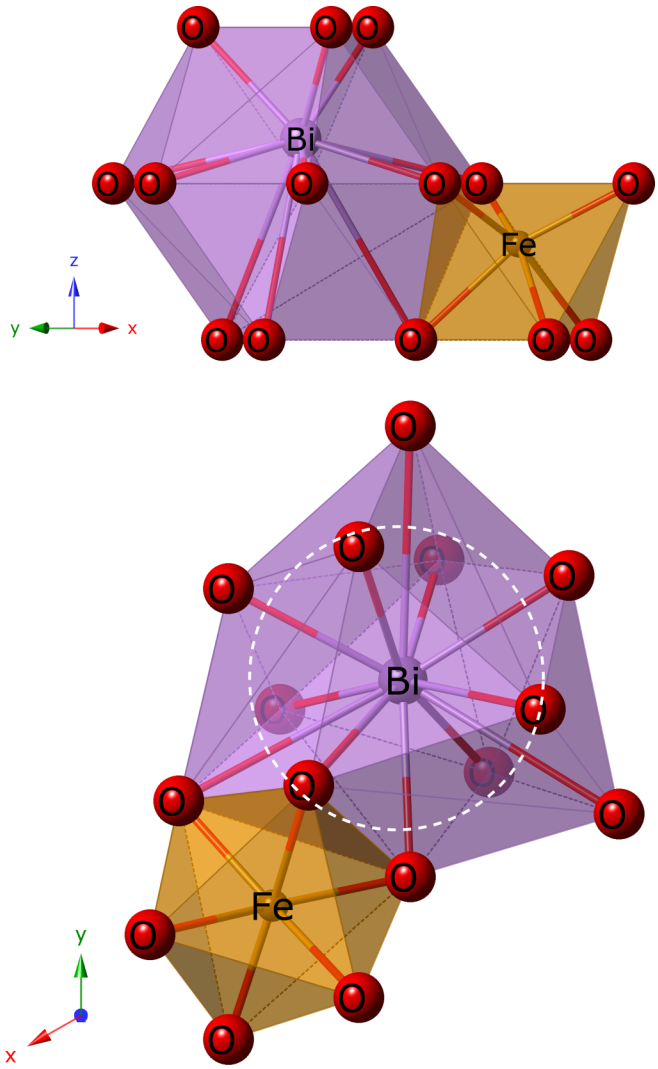

FIG. 6. Schematic illustration of FeO_6 and BiO_{12} polyhedra viewed along two axes. The white circle encompasses the shorter six Bi–O distances.

We should comment about the role of magnetic scattering. Because the magnetic part of the Fe atoms are in the outer atomic shells, the value of the magnetic form factor decreases quickly with Q. For the same reason, without any special attention peaks in the PDF from magnetic correlations will be extremely broad and essentially indistinct. By not accounting for magnetic scattering within the reduction of the total scattering data, corrections to make the data consistent with the known density and atomic composition [that is, to give the expected slopes in the low-Q and low-r parts of the $Qi(Q)$ and $D(r)$ functions respectively], the data reduction method will have treated the magnetic diffuse scattering as noise and subtracted it from the final form of the $i(Q)$ function. The only part of the final data sets therefore that will contain magnetic scattering is the Bragg profile, where there is one strong magnetic peak that could easily be excluded from the RMC analysis and some much weaker peaks.

RMC modeling was performed using the RMC profile program [41], which is optimized for applying the method to crystalline materials. The method uses the traditional

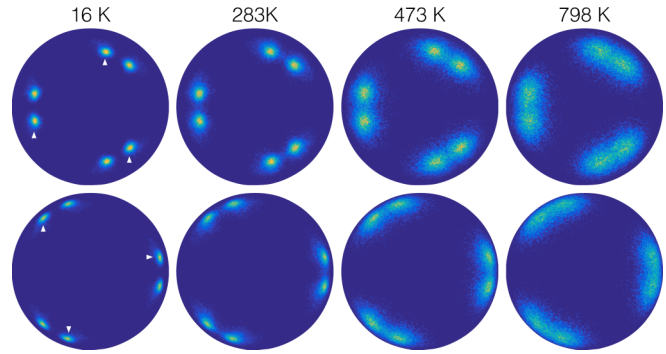

FIG. 7. Orthographic projection of the orientational distribution function of all Fe–O bonds in $BiFeO_3$ at four temperatures. Dark blue corresponds to no bonds in that orientation, and yellow shows the maximum value of the distribution function. The upper and lower plots show projections viewed down the [001] and [00$\bar{1}$] directions. The plots show vectors from two distinct but symmetrically related orientations of the FeO_6 octahedra, meaning that the plots show 12 rather than 6 vectors. The peaks in the distribution function from one distinct set of octahedra are indicated by the white triangles in the plots for 16 K.

Metropolis Monte Carlo algorithm to move atoms, using an "energy" function that reflects the agreement between calculated and measured functions $i(Q)$, $D(r)$ and the Bragg profile. Specifically, writing the measured (observed) and calculated value of any function at data point i in data set j as $y_{i,j}^{\mathrm{obs}}$ and $y_{i,j}^{\mathrm{calc}}$ respectively, we define the function

$$\chi^2 = \sum_j \sum_i \left(y_{i,j}^{\mathrm{obs}} - y_{i,j}^{\mathrm{calc}}\right)^2 / \sigma_j, \tag{6}$$

where σ_j provides a weighting for a specific data set and represents the statistical accuracy of the data set, albeit not on a point-by-point basis. Atomic moves are proposed at random (random atom, random movement subject to a

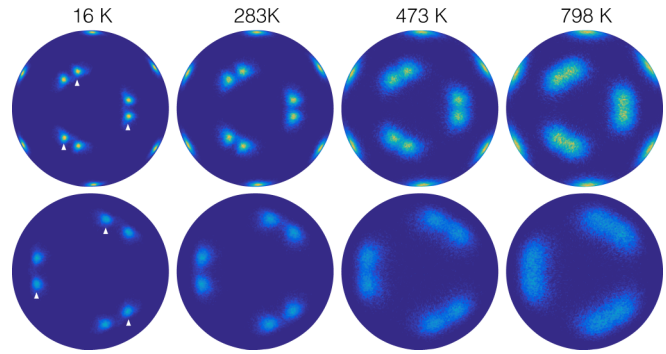

FIG. 8. Orthographic projection of the orientational distribution function of all Bi–O bonds in $BiFeO_3$ at four temperatures. The upper and lower plots show projections viewed down the [001] and [00$\bar{1}$] directions. As noted in the caption to Fig. 7 the plots show vectors from two distinct but symmetrically related orientations of the BiO_{12} cuboctahedra. As in Fig. 7 we identify the peaks in the distribution function from one set of symmetrically identical cuboctahedra, but note that for the zenith angles just less than 90° the two distinct cuboctahedra have peaks with identical polar angles. This point can be seen by inspection of Fig. 6.

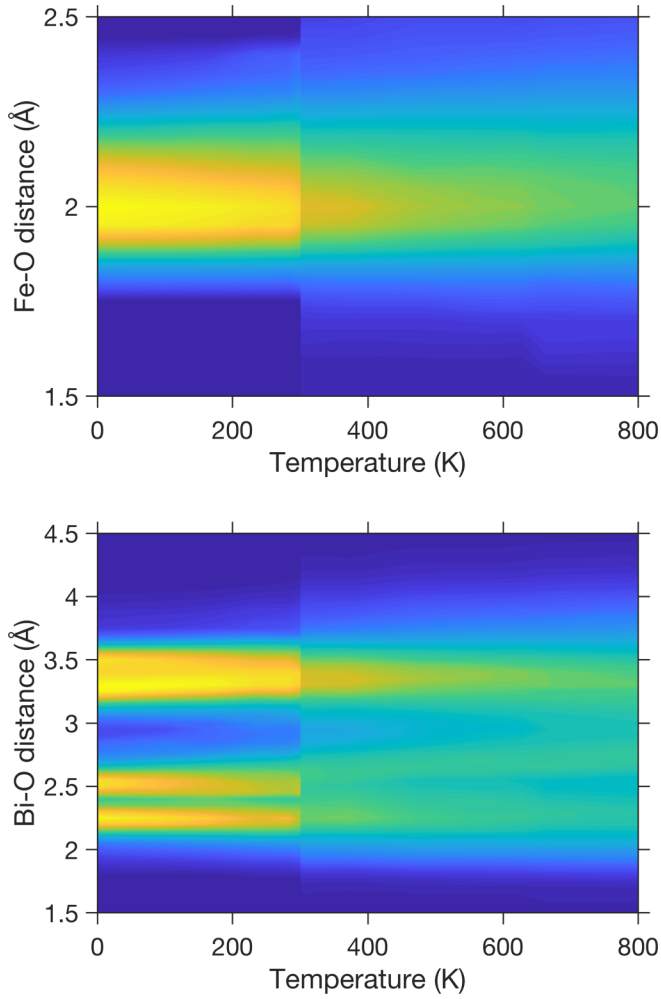

FIG. 9. Color maps of the distributions of Fe–O and Bi–O distances. The difference in clarity between the low- and high-temperature data reflects the relatively high background from the furnace; see the discussion in the text.

maximum value of the atomic displacement). A move that lowers the value of χ^2 is accepted, but a move that raises the value of χ^2 by an amount $\Delta\chi^2$ is accepted with probability $\exp(-\Delta\chi^2/2)$. In order to prevent atoms moving too far away from their local topology within the crystal structure, we employed distance windows, which impose a minimum and maximum atomic separation between pairs of atoms defined by a prior neighbor list [42].

The supercell configurations were set up with orthogonal edge sizes of around 48, 50, and 56 Å, containing 10 800 atoms; this was a $5 \times 9 \times 4$ supercell of the C-centered orthorhombic cell obtained by transformation of the hexagonal unit cell, with lattice vectors $2\mathbf{a}_h + \mathbf{b}_h$, $\mathbf{b}_h$, $\mathbf{c}_h$. The starting positions were generated directly from the crystal structures generated by Rietveld refinement. Each RMC analysis was run for long enough to give more than 200 accepted moves per atom. Maximum atomic moves were of size 0.05 Å. Convergence of the RMC simulations was checked by monitoring the value of χ^2 as defined above.

III. AVERAGE STRUCTURE FROM RIETVELD REFINEMENT

Rietveld refinement of data collected over the whole temperature range measured showed an excellent fit to the $R3c$ model consistent with previous studies [4,13,14]. A sample fit to the data, namely for the data at 161 K, is shown in Fig. 2.

Refined values for the structural parameters for all temperatures are given in Tables I (unit cell and fractional coordinates) and II (atomic displacement parameters). The lattice parameters are plotted as functions of temperature in Fig. 3. Both a and c vary smoothly with temperature, with no indications of anomalies or strain associated with the magnetic phase transition. The results for both a and c are consistent with previous results [4,14]. Both lattice parameters show the usual change from linear variation with temperature at around 150 K. As discussed in the Sec. I, this region has previously been suggested to correspond to potential changes in the magnetic and/or atomic structures, and anomalous phonon behavior. However, no apparent effects are seen in the data presented in Fig. 3.

IV. ANALYSIS FROM THE REVERSE MONTE CARLO METHOD

A. RMC data refinement

The RMC fits to the three functions used in the RMC analysis, namely the Bragg scattering profile, the scattering function $i(Q)$, and the PDF $D(r)$, is shown for all temperatures in Fig. 4. It can be seen that in all cases the quality of the fitting is good. It should be noted that the ripples in the experimental $i(Q)$ function were artificially created within

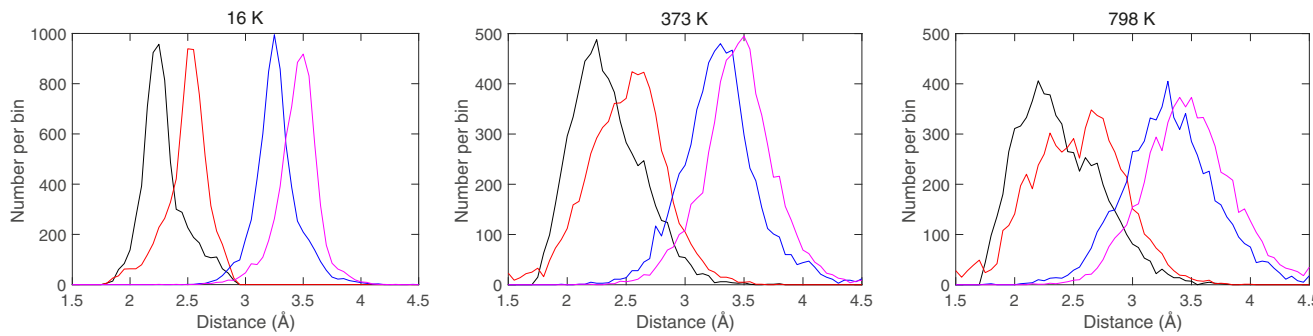

FIG. 10. Histograms of the four distinct Bi–O near-neighbor distances at three temperatures.

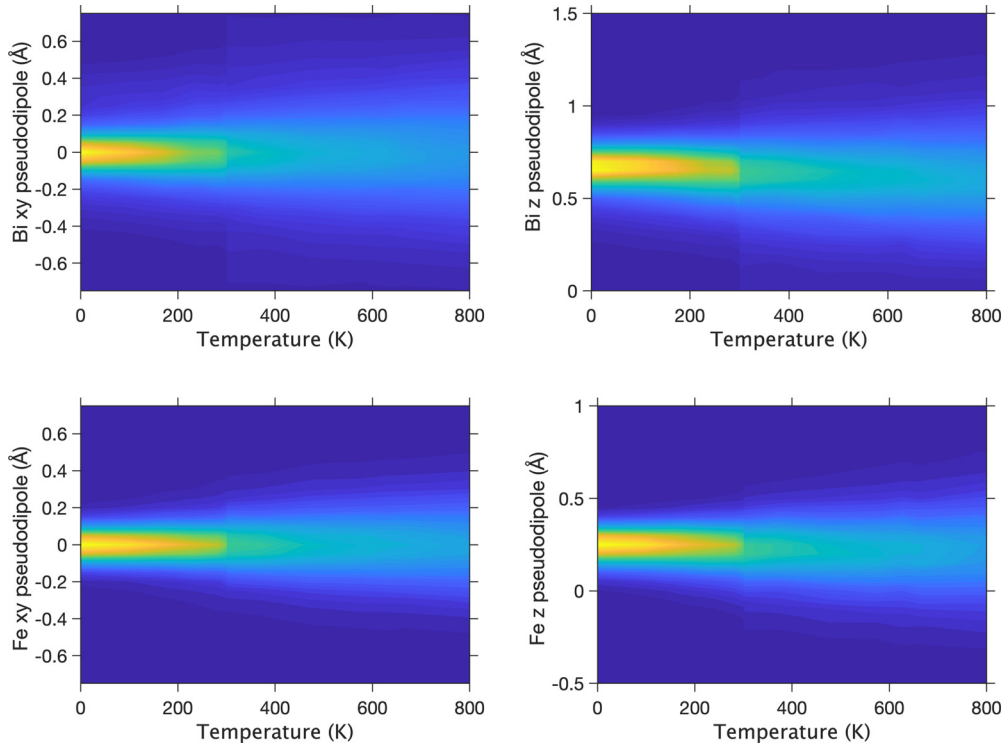

FIG. 11. Color contour maps of the distributions of pseudodipole moments associated with the FeO_6 and BiO_{12} polyhedra. The dipole moments have units of Å. As in Fig. 9, the difference in clarity between the low- and high-temperature data reflects the relatively high background from the furnace.

the RMC method. Because the $D(r)$ function calculated from the RMC configuration has a maximum value of r, as set by the size of the configuration, the calculated $i(Q)$ function obtained by Fourier transform of $D(r)$ will contain truncation ripples. Therefore to facilitate an accurate comparison between the calculated and experimental $i(Q)$ functions, the experimental $Qi(Q)$ functions were automatically convolved with the Fourier transform of the box function of the same maximum value of r. For each temperature we performed ten independent RMC simulations, and all results are averaged over all final configurations.

B. Average structure from RMC

We projected the position of all atoms in the configuration back into one unit cell, and from the distribution of atomic positions we calculated the average atomic positions and mean-square anisotropic displacements from the associated distribution. An example of this projection, from the RMC analysis performed on the data collected at a temperature of 473 K, is shown in Fig. 5. From the figure, and consistent with the results from Rietveld analysis shown in Table II, we can see that the atomic displacement parameters (which in this case represent thermal motions) of O and Bi atoms are larger than for the Fe atoms.

C. Local structure from RMC: Atomic structures of the FeO_6 and BiO_{12} polyhedra

Here we focus on the fluctuations in the FeO_6 and BiO_{12} polyhedra. As the crystallographic analysis shows (above, and Refs. [4] and [14]), at all temperatures both polyhedra are significantly distorted from their highly symmetric form of the ideal cubic phase. The average local coordination of the Fe and Bi atoms is shown in Fig. 6, where the distortions are clear. In particular, both polyhedra have lost their center of symmetry and therefore have a local dielectric polarization. In the case of the BiO_{12} polyhedra, not only is there a distortion of the shape but also a significant change in Bi–O distances, six having shorter distances (2.2 and 2.5 Å) and six having longer distances (3.2 and 3.5 Å). This is consistent with asymmetric bonding expected for the BiO_{12} polyhedra as a result of hybridization between the Bi $6s^2$ lone pair and the $6p$ orbitals [43].

Our analysis here is focused on the orientations and lengths of the Fe–O and Bi–O bonds, how both their mean values and associated fluctuations change with temperature. The orientational distributions of the Fe–O and Bi–O bonds are shown as orthographic projections in Figs. 7 and 8 respectively. These diagrams correspond to the vertical axis being parallel to the crystallographic [001], with separate diagrams showing views from positive and negative directions. Data are shown for four temperatures between 16 and 800 K. For both cases the diagrams include the two sets of symmetrically related bonds in different polyhedra. Thus we see pairs of peaks in the distribution functions. The advantage of showing both polyhedra in one diagram is that the angular separation between related pairs reflects the extent to which the symmetry of the parent cubic phase has been broken through bond and polyhedral reorientation (noting that both subtend the same angle with respect to the vertical axis, so the angular separation is directly about the vertical).

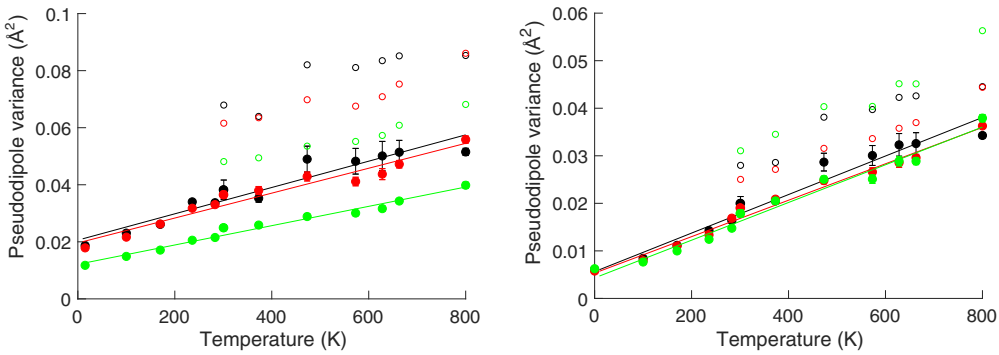

FIG. 12. Variances of the pseudodipole moments associated with the BiO_{12} (left) and FeO_6 (right) polyhedra. Black, red, and green points correspond to directions x, y, z, where we expect the data for the x and y directions to have the same values. The open circles represent the RMC results without corrections. The filled circles below a temperature of 300 K are similarly the RMC results without corrections. The filled circles for temperatures above 300 K are obtained by subtracting from the RMC results a constant offset obtained by subtracting the difference in the two values at 300 K obtained for samples within the CCR and furnace, accounting for the problems described in the text in relation to Fig. 9. The straight lines are guides to the eye to show that the corrected data are consistent with linear increases with temperature.

A striking point from Figs. 7 and 8 is that the angular separations of the median bond orientations in the distribution functions for symmetrically related pairs change very little with temperature. This means that there are almost no changes in the mean orientations of either Fe–O or Bi–O bonds, and hence no rotations of the corresponding polyhedra, over the wide temperature range represented in the data. However, the extent of thermal motion associated with the orientations of the bonds grows considerably on heating, as seen in the wide angular distribution of the bond vectors. Indeed, the fluctuations become as large as the angular separation of the pairs of symmetrically related peaks. We will comment more on this later in this section.

Second we consider the fluctuations in the bond distances. In Fig. 9 we show a color map of the distribution of Fe–O and Bi–O distances as a function of temperature. As an (important) aside, this figure shows one factor that we were unable to eliminate from our analysis, namely that the data obtained within the CCR and furnace show some systematic differences that feed through to slightly more disorder coming into the RMC configurations of the higher-temperature data. This probably arises from effects due to the relatively large background from the furnace.

In the case of the Fe–O bond, there are actually two symmetrically distinct distances of around 2.0 and 2.1 Å at low temperature, but with larger fluctuations than the difference in distances the overall distribution appears to be single-peaked in the color map. On the other hand, there is a much wider spread of symmetrically distinct Bi–O distances, at around 2.3, 2.5, 3.3, and 3.5 Å. We plot the distribution functions for these four distinct bond distances for three temperatures in Fig. 10. A similar broad distribution of Bi–O distances was seen in the room-temperature PDF study of $BiFeO_3$-$PbTiO_3$ solid solutions [30], and in La and La/Tb doped $BiFeO_3$ materials [24]. Similar to the orientations of bond vectors, two points emerge from the histograms of instantaneous distances. First is that there is little change in the midpoints of the distribution of each bond distance over the whole temperature range, just as there is no clear change in the median values of the bond orientation distributions. Second is that there is a great deal of thermal motion. Indeed, the spread of distances at high temperature significantly exceeds the differences in mean positions.

Thus we see from taking all the data together that the average sizes, shapes, and orientations of both types of coordination polyhedra remain virtually unchanged on heating from the lowest to highest temperature in this study. On the other hand, the same data show significant thermally induced fluctuations, with the fluctuations becoming as large as the distortions of the average structure from the ideal cubic parent structure. This is consistent with the INS data, which show a considerable broadening of the peaks in the phonon density of states with increasing temperature, particularly for the modes associated with motions of the bismuth atoms [11,44], which might suggest the existence of significant anharmonicity. Likewise, resonant ultrasound spectroscopy has suggested increasing disorder with increasing temperature [19].

There is one surprising aspect about the lack of change in the average structure across the temperature range of our data. Normally, on heating towards a phase transition to a higher-symmetry parent structure (in this case the relevant structure, in terms of symmetry group-subgroup relationships, is the γ phase of nominally cubic symmetry) the structure will transform towards that of the high-symmetry phase with the distortion becoming smaller on heating. Although one might argue that the highest temperature in our dataset falls short of the transition temperature by a considerable amount (300 K), in the sense of a second-order Landau approximation (which is relevant in the case of ferroelectric phase transitions) where the ferroelectric distortions will vary with temperature as $(T - T_c)^{1/2}$, we might expect to see a reduction in the overall distortions by around 50%. This will not just be true for the dipolar displacements of the cations from the centers of their polyhedra, but also true of the distortions and rotations of the polyhedra. We can cite, for comparison, our previous RMC study of the phase transition in $SrTiO_3$, which showed clearly changes upon heating towards the phase transition [45]. The constancy of the structure across a wide range of temperatures is one of the curious aspects of the phase transition behavior of $BiFeO_3$.

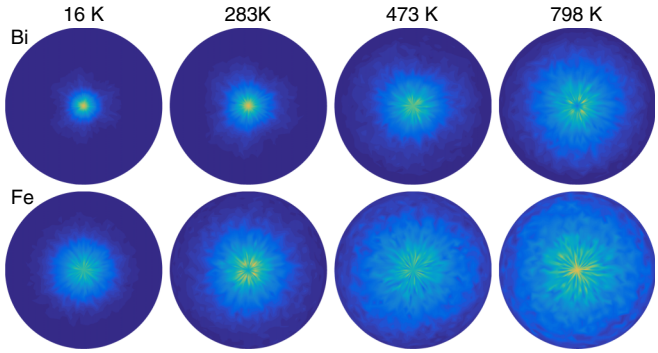

FIG. 13. Orthographic projection of the orientational distribution function of the local pseudodipoles associated with the BiO_{12} (top) and FeO_6 (bottom) polyhedral for four temperatures.

D. Local structure from RMC: Dipolar fluctuations of the FeO_6 and BiO_{12} polyhedra

In this final part we analyze the distortions of the FeO_6 and BiO_{12} polyhedra in terms of local pseudodipole moments, calculated by summing over the bond vectors centered on the cation. What we call the "pseudodipole moment" is thus effectively the displacement of the central cation from the centroid of the polyhedron formed by its surrounding oxygen anions. This provides a convenient measure of the local moment without relying on any specific model of the charge distribution. The existence of these dipoles can be seen in the local structure diagrams in Fig. 6. We calculated the size distributions of the pseudodipole moments in the [001] direction and in the orthogonal directions as functions of temperature, and present the results as color maps in Fig. 11.

The mean moment of the pseudodipole moments in the directions normal to [001] is zero as expected, and we see growing fluctuations of the pseudodipole moments on heating. On the other hand, there is a nonzero average moment for both polyhedra in the [001] direction, as is clearly seen in Fig. 11. What is striking is that the mean pseudodipole moments of both types of polyhedra do not change significantly with temperature even though there is a significant effect of thermal motion. Indeed, the fluctuations are almost as large as the average moments at the highest temperature. The variances of the values of the pseudodipole moments of both polyhedra are shown in Fig. 12, where we see a simple linear increase with temperature as normally expected for harmoniclike thermally induced motions.

Finally we consider the distribution of orientations of the pseudodipole moments, which we show in orthographic projections in Fig. 13. At lowest temperature it can be seen that the distribution is very tight, and the shape of the distribution reflects slightly the threefold symmetry of the crystal. However, on heating there is a wide distribution in the orientational distribution, even wider than the bond orientations, reflecting very large local fluctuations. This could be consistent with subtle fluctuations in structure as proposed in the inelastic neutron-scattering data of Ref. [11].

V. CONCLUSION

The key result of this study is that the average atomic structure of $BiFeO_3$ remains robustly stable across the temperature range 16–800 K, in spite of the existence of large thermal fluctuations at the higher temperatures. This is represented in analysis of bond lengths, bond orientations, local coordination, and local dipole moments. The RMC analysis in this study has shown that the local bonds around the Bi cation can fluctuate by a very large fraction, around 1 Å with bond lengths of 2.5–3 Å, yet the averages barely change. In the literature are several reports of apparent phase transitions and other thermal anomalies at various temperatures [1,11,15–17,19,22], but no structural anomalies are seen in this study in either the average or local structure. In this sense our results are consistent with the results of several diffraction studies [4,13,14]. In particular we see no effects from the magnetic phase transition in any of the features of the local structure. However, we note that no structural phase transition is expected at T_N with $R3c$ symmetry adopted both above and below T_N. Furthermore, there is no sign over the temperature range of this study of the onset of the phase transition on heating towards the paraelectric phase, such as a change in the local structure towards lower average distortion. Likewise, we see no evidence below room temperature to support either a structural phase transition or a significant change in the magnetic behavior. Thus we conclude that all anomalies below room temperature reported in previous studies using indirect probes are unlikely to be seeing changes in the atomic structure of the bulk, or in local fluctuations, and thus are more likely to arise from effects generated at surfaces and interfaces (including domain walls and grain boundaries). Such effects would not have noticeable impacts on the scattering data and resultant PDF.

ACKNOWLEDGMENTS

We are grateful to ISIS for provision of neutron beam time (Projects No. RB1610460 and No. RB1310476). J.D. is grateful to the China Scholarship Council and Queen Mary University of London for financial support. This research utilized Queen Mary's Apocrita HPC facility [46], supported by QMUL Research-IT and funded by EPSRC Grants No. EP/K000128/1 and No. EP/K000233/1.

[1] G. Catalan and J. F. Scott, Adv. Mater. **21**, 2463 (2009).
[2] D. C. Arnold, Ultrasonics, Ferroelec., Freq. Cont. **62**, 62 (2015).
[3] I. Sosnowska, T. Peterlin-Neumaier, and E. Steichele, J. Phys. C **15**, 4835 (1982).
[4] D. C. Arnold, K. S. Knight, F. D. Morrison, and P. Lightfoot, Phys. Rev. Lett. **102**, 027602 (2009).
[5] R. Palai, R. S. Katiyar, H. Schmid, P. Tissot, S. J. Clark, J. Robertson, S. A. T. Redfern, G. Catalan, and J. F. Scott, Phys. Rev. B **77**, 014110 (2008).
[6] D. C. Arnold, K. S. Knight, G. Catalan, S. A. T. Redfern, J. F. Scott, P. Lightfoot, and F. D. Morrison, Adv. Funct. Mater. **20**, 2116 (2010).

[7] S. M. Selbach, M. A. Einarsrud, and T. Grande, Chem. Mater. **21**, 169 (2009).

[8] T. Rojac, A. Bencan, B. Malic, G. Totuncu, J. L. Jones, J. E. Daniels, and D. Damjanovic, J. Am. Ceram. Soc. **97**, 1993 (2014).

[9] A. Perejón, P. E. Sánchez-Jiménez, J. M. Criado, and L. A. Péres-Maqueda, J. Phys. Chem. C **118**, 26387 (2014).

[10] D. C. Palmer, Z. Kristallogr. - Cryst. Mater. **230**, 559 (2015).

[11] O. Delaire, M. B. Stone, J. Ma, A. Huq, D. Gout, C. Brown, K. F. Wang, and Z. F. Ren, Phys. Rev. B **85**, 064405 (2012).

[12] J. A. Schneeloch, Z. Xu, J. Wen, P. M. Gehring, C. Stock, M. Matsuda, B. Winn, G. Gu, S. M. Shapiro, R. J. Birgeneau, T. Ushiyama, Y. Yanagisawa, Y. Tomioka, T. Ito, and G. Xu, Phys. Rev. B **91**, 064301 (2015).

[13] J. Herrero-Albillos, G. Catalan, J. A. Rodriguez-Velamazan, M. Viret, D. Coulson, and J. F. Scott, J. Phys.: Condens. Matter. **22**, 256001 (2010).

[14] A. Palewicz, I. Sosnowska, R. Przeniosło, and A. W. Hewat, Acta Phys. Pol. A **117**, 296 (2010).

[15] M. Cazayous, Y. Gallais, A. Sacuto, R. de Sousa, D. Lebeugle, and D. Colson, Phys. Rev. Lett. **101**, 037601 (2008).

[16] M. K. Singh, R. S. Katiyar, and J. F. Scott, J. Phys.: Condens. Matter **20**, 252203 (2008).

[17] B. Ramachandran, A. Dixit, R. Naik, and M. S. R. Rao, J. Appl. Phys. **110**, 104105 (2011).

[18] J. Hlinka, J. Pokorny, S. Karimi, and I. M. Reaney, Phys. Rev. B **83**, 020101(R) (2011).

[19] R. Jarrier, X. Marti, J. Herrero-Albillos, P. Ferrer, R. Haumont, P. Gemeiner, G. Geneste, P. Berthet, T. Schulli, P. Cevc, R. Blinc, S. S. Wong, T. J. Park, M. Alexe, M. A. Carpenter, J. F. Scott, G. Catalan, and B. Dkhil, Phys. Rev. B **85**, 184104 (2012).

[20] N. Domingo, J. Narvaez, M. Alexe, and G. Catalan, J. Appl. Phys. **113**, 187220 (2013).

[21] T. Yang, C. Wang, X. Zhang, Y. Feng, H. Guo, K. Jin, X. Gao, Z. Li, and X. Li, Appl. Phys. Lett. **105**, 202901 (2014).

[22] J. W. Lin, J. S. Gardner, C.-W. Wang, G. Deng, C. M. Wu, V. K. Peterson, and J. G. Lin, AIP Adv. **7**, 055836 (2017).

[23] B. Jiang and S. M. Selbach, J. Solid State Chem. **250**, 75 (2017).

[24] Y. Yoneda, K. Yoshii, S. Kohara, S. Kitagawa, and S. Mori, Jpn. J. Appl. Phys. **47**, 7590 (2008).

[25] Y. Yoneda, K. Yoshii, H. Saitoh, and J. Mizuki, Ferroelectrics **355**, 119 (2007).

[26] S. Unruan, M. Unruan, T. Monnor, S. Priya, and R. Yimnirun, J. Am. Ceram. Soc. **98**, 3291 (2015).

[27] N. Ishimatsu, T. Watanabe, K. Oka, M. Azuma, M. Mizumaki, K. Nitta, T. Ina, and N. Kawamura, Phys. Rev. B **92**, 054108 (2015).

[28] S. Unruan, S. Srilomsak, S. Priya, P. Jantaratana, S. Rujirawat, and R. Yimnirun, Ceram. Int. **41**, 4087 (2015).

[29] Y. Yoneda, Y. Kitanaka, Y. Noguchi, and M. Miyayama, Phys. Rev. B **86**, 184112 (2012).

[30] I. Levin, V. Krayzman, M. G. Tucker, and J. C. Woicik, Appl. Phys. Lett. **104**, 242913 (2014).

[31] A. C. Hannon, Nucl. Instrum. Methods Phys. Res., Sect. A **551**, 88 (2005).

[32] M. T. Dove, A. E. Phillips, J. Du, D. A. Keen, D. C. Arnold, and M. G. Tucker, Total scattering from multiferroic bismuth ferrite, STFC ISIS Neutron and Muon Source (2013), doi: 10.5286/ISIS.E.RB1310476.

[33] M. T. Dove, A. E. Phillips, J. Du, D. A. Keen, D. C. Arnold, and M. G. Tucker, Total scattering from multiferroic bismuth ferrite at high temperatures, STFC ISIS Neutron and Muon Source (2016), doi: 10.5286/ISIS.E.RB1610460.

[34] O. Arnold, J. Bilheux, J. Borreguero, A. Buts, S. Campbell, L. Chapon, M. Doucet, N. Draper, R. F. Leal, M. Gigg, V. Lynch, A. Markvardsen, D. Mikkelson, R. Mikkelson, R. Miller, K. Palmen, P. Parker, G. Passos, T. Perring, P. Peterson *et al.*, Nucl. Instrum. Methods Phys. Res., Sect. A **764**, 156 (2014).

[35] A. C. Larson and R. B. V. Dreele, Los Alamos National Laboratory Report No. LAUR 86–748, 2001.

[36] B. H. Toby, J. Appl. Crystallogr. **34**, 210 (2001).

[37] A. K. Soper, Rutherford Appleton Laboratory Technical Report No. RAL-TR-2011-013, 2011.

[38] A. C. Hannon, W. S. Howells, and A. K. Soper, *Neutron Scattering Data Analysis*, Institute of Physics Conference Series No. 107 (IOP Publishing Ltd., 1990), pp. 193–211.

[39] E. Lorch, J. Phys. C: Solid State Phys. **2**, 229 (1969).

[40] E. Lorch, J. Phys. C: Solid State Phys. **3**, 1314 (1970).

[41] M. G. Tucker, D. A. Keen, M. T. Dove, A. L. Goodwin, and Q. Hui, J. Phys.: Condens. Matter **19**, 335218 (2007).

[42] Window ranges used were 3.5–4.66 Å for Fe–Fe, 1.76–2.5 Å for Fe–O, 2.5–4.7 Å for Fe–Bi, 1.75–5 Å for Bi–O, 2–5 Å for O–O, and 3.3–4.8 Å for Bi–Bi.

[43] J.-G. Park, M. D. Le, J. Jeong, and S. Lee, J. Phys.: Condens. Matter **26**, 433202 (2014).

[44] M. Zbiri, H. Schober, N. Choudhury, R. Mittal, S. L. Chaplot, S. J. Patwe, S. N. Achary, and A. K. Tyagi, Appl. Phys. Lett. **100**, 142901 (2012).

[45] Q. Hui, M. G. Tucker, M. T. Dove, S. A. Wells, and D. A. Keen, J. Phys.: Condens. Matter **17**, S111 (2005).

[46] T. King, S. Butcher, and L. Zalewski, Apocrita - High Performance Computing Cluster for Queen Mary University of London (2017), doi: 10.5281/zenodo.438045.